Acta Pharmaceutica Sinica B 2024;14(11):5037−5052

Chinese Pharmaceutical Association
Institute of Materia Medica, Chinese Academy of Medical Sciences

Acta Pharmaceutica Sinica B

www.elsevier.com/locate/apsb
www.sciencedirect.com

ORIGINAL ARTICLE

Spatiotemporally responsive cascade bilayer microneedles integrating local glucose depletion and sustained nitric oxide release for accelerated diabetic wound healing

Yongnian Zeng [a], Chenyuan Wang [a], Jiapeng Lei [a], Xue Jiang [a], Kai Lei [b,c], Yinli Jin [a], Tianshu Hao [a], Wen Zhang [a], Jianying Huang [b,c,*], Wei Li [a,c,d,*]

[a]*Department of Thyroid and Breast Surgery, Zhongnan Hospital of Wuhan University, School of Pharmaceutical Sciences, Wuhan University, Wuhan 430071, China*
[b]*Clinical Trial Center of Zhongnan Hospital, Wuhan University, Wuhan 430071, China*
[c]*Tumor Precision Diagnosis and Treatment and Translational Medicine Hubei Engineering Research Center, Wuhan 430071, China*
[d]*TaiKang Center for Life and Medical Sciences, Wuhan University, Wuhan 430071, China*

Received 26 February 2024; received in revised form 24 May 2024; accepted 25 May 2024

KEY WORDS

Microneedle;
Wound healing;
Drug delivery;
Sustained release;
Nitric oxide;
Glucose depletion;
Glucose oxidase;
Nanoparticles

Abstract High glucose level, bacterial infection, and persistent inflammation within the microenvironment are key factors contributing to the delay of diabetic ulcers healing, while traditional therapeutic methods generally fail to address these issues simultaneously. Here, we present a spatiotemporally responsive cascade bilayer microneedle (MN) patch for accelerating diabetic wound healing *via* local glucose depletion and sustained nitric oxide (NO) release for long-term antibacterial and anti-inflammatory effects. The MN patch (G/AZ-MNs) possesses a degradable tip layer loading glucose oxidase (GOx), as well as a dissolvable base layer encapsulating L-arginine (Arg)-loaded nanoparticles (NPs). After wound administration, the base part rapidly dissolved, resulting in prompt separation of the MN tip within the wound tissue, which subsequently responded to the overexpressed matrix metalloproteinase-9 (MMP-9) in diabetic lesions, leading to the responsive release of GOx. The released enzyme catalyzed glucose into gluconic acid and hydrogen peroxide (H_2O_2), which not only reduced glucose level within the diabetic wound, but also initiated the cascade reaction between H_2O_2 with the

*Corresponding authors.
E-mail addresses: huangjianying@znhospital.cn (Jianying Huang), weili.mn@whu.edu.cn (Wei Li).
Peer review under the responsibility of Chinese Pharmaceutical Association and Institute of Materia Medica, Chinese Academy of Medical Sciences.

https://doi.org/10.1016/j.apsb.2024.06.014

Arg that was released from NPs, thereby achieving continuous production of NO for 7 days. Our findings demonstrate that a single administration of the MN patch could effectively heal non-infected or biofilm-infected diabetic wounds with the multifunctional properties.

1. Introduction

Currently, about half a billion people are living with diabetes, and it is estimated that the diabetes number will increase to 1.31 billion by 2050 worldwide[1,2]. Diabetic foot ulcers (DFUs) represent a prevalent complication of diabetes and stand as a significant catalyst for amputations among individuals affected by diabetes[3,4]. The widespread occurrence of DFUs exerts a substantial financial strain on both the families of diabetic patients and the healthcare system at large[5,6]. Skin wound healing is an intricate and dynamic process comprising three distinct phases: inflammation, proliferation, and remodeling[7,8]. However, high glucose level within the diabetic wound environment generally hinders the transition of wound tissue towards the crucial remodeling phase, since the prolonged hyperglycemia exerts inhibitory effects on vascularization and the expression of diverse growth factors, leading to the development of chronic and nonhealing wounds[9]. Additionally, excessive inflammation at the wound, typically caused by bacterial infection, is another key factor that contributes to the impairment of tissue regeneration[10-12]. Consequently, the reduction of glucose concentration and delivery of antibacterial and anti-inflammatory agents in the local environment of wound beds have emerged as novel therapeutic approaches in the treatment of chronic diabetic wounds[13-15].

Despite great advancements in the development of glucose-depletion systems to consume glucose for the promotion of diabetic wound healing, such as hydrogels[16], nanomaterials[17], or microparticles[18], which are topically applied on wounds, the developed platforms usually suffer from limited drug penetration into deep tissue layer, thereby resulting in compromised efficacy in adjusting hyperglycemia condition at deep wound tissues. Nitric oxide (NO) has been proved to be safe and effective for diabetic wound therapy as an antibacterial and anti-inflammatory agent, because NO is an endogenous gas transmitter and involves the regulation of various important wound healing processes, including anti-inflammation, anti-infection, cell migration, collagen formation, and angiogenesis[19,20]. Therefore, a variety of NO delivery systems have also been widely studied for DFUs treatment, some of which have even been investigated in clinical trials[19,21,22]. However, their significant improvement on wound healing is largely limited by the reactive chemical properties and short half-life characteristic of NO molecule[23,24], and the developed systems usually cannot achieve sustained release of NO at wounds. As a result, the strategy of glucose depletion at deep wounds or sustained NO supply inside the wound tissue has been considered potential to address the delay of diabetic wound healing, but the combination of these two strategies has not been reported so far.

Here, we report a spatiotemporally responsive cascade bilayer MN patch, designed to address wound repair through effective glucose depletion and sustained release of NO at wounds (Fig. 1). This extraordinary MN patch, denoted as G/AZ-MN patch, possesses two components: 1) the tip layer that is composed of MMP-9 degradable gelatin methacrylate (GelMA) encapsulating glucose oxidase (GOx); and 2) the base layer that is made from dissolvable hyaluronic acid (HA) encapsulating acid-responsive L-arginine-loaded zeolitic imidazolate framework nanoparticles (Arg@ZIF-8 NPs) (Fig. 1A). Upon application to the wound area, the water-soluble base layer rapidly dissolved, thereby releasing the Arg@ZIF-8 NPs and simultaneously implanting the degradable GOx-loaded tip layer in the wound tissue. The GelMA-tip of MNs underwent subsequent degradation catalyzed by the enzyme of MMP-9 that is highly expressed in diabetic wounds, resulting in the release of GOx into the wound tissue. The liberated GOx enzyme then catalyzed the oxidation of glucose, generating H_2O_2 and lowering the pH *via* gluconic acid production within the wound site. This dual action not only caused a reduction of the local glucose level but also initiated a cascade reaction that triggered the degradation of the pH-responsive Arg@ZIF-8 NPs, causing the release of Zn^{2+} ions and Arg. The released Zn^{2+} effectively impeded the formation of bacterial biofilms, while Arg reacted with H_2O_2 to continuously produce NO, thereby playing critical roles in wound healing promotion through antibacterial and anti-inflammatory effects (Fig. 1B). Due to such attractive features, the application of the G/AZ-MN patch exhibited superior therapeutic efficacy in wound healing, not only in non-infected diabetic wounds but also in diabetic wounds that were infected by *Staphylococcus aureus* (*S. aureus*). We believe that the MN patch will provide a promising and effective alternative to current therapies for the treatment of DFUs. Here, we present this MN patch and study its performance *in vitro*, *ex vivo*, and *in vivo*.

2. Materials and methods

2.1. Materials

The reagents of 2-methylimidazole, L-arginine (Arg), GOx, 2-hydroxy-4′-(2-hydroxyethoxy)-2-methylpropiophenone, erythromycin (EM), streptozotocin and methacrylate gelatin were purchased from Aladdin Reagent Co. (Shanghai, China). Fluorescein 5-isothiocyanate, rhodamine B (RB), bovine serum albumin (BSA), $Zn(NO_3)_2{\cdot}6H_2O$, and sucrose were purchased from Macklin Biochemical Technology Co. (Shanghai, China). Hyaluronic acid (HA, molecular weight, 10 kDa) was purchased from Meilun Biotechnology Co. (Dalian, China). Methanol, gelatin, agarose, glucose, and H_2O_2 were purchased from Sinopharm Chemical Reagent Co. (Shanghai, China). Matrix metalloproteinases-9 (MMP-9) was purchased from Sigma−Aldrich (Missouri, USA). Luria−Bertani (LB) nutrient

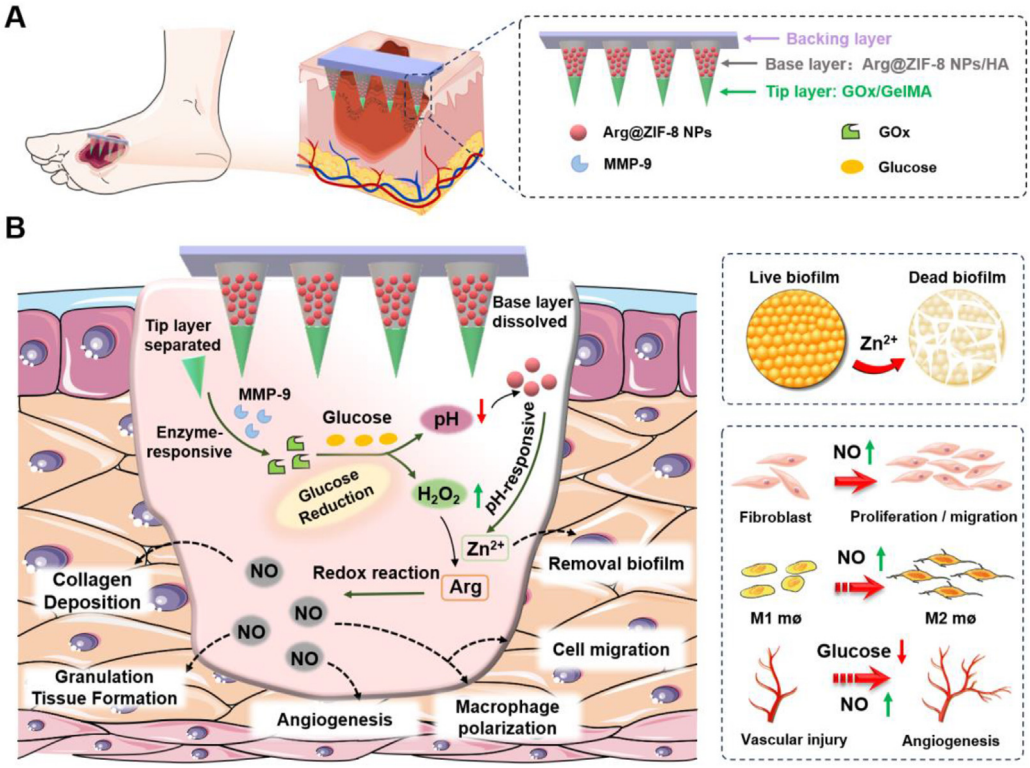

Figure 1 Schematic illustration of the microenvironment-responsive bilayer G/AZ-MNs for promoting diabetic wound healing through glucose depletion and sustained release of NO. (A) The design of bilayer G/AZ-MNs. (B) The application of bilayer G/AZ-MNs to diabetic wounds.

broth and LB nutrient agar were purchased from Hopebio Biotechnology Co. (Qingdao, China). LIVE/DEAD bacLight bacterial viability kits were purchased from Thermo Fisher Scientific (Waltham, USA). Dulbecco's modified Eagle medium (DMEM), fetal bovine serum, and penicillin-streptomycin antibiotics were obtained from Procell Life Science & Technology Co. (Wuhan, China). 3-[4,5-Dimethylthiazol-2-yl]-2,5 diphenyl tetrazolium bromide (MTT) cell proliferation and cytotoxicity assay kit, Calcein/PI cell viability/cytotoxicity assay kit, hydrogen peroxide content detection kit, NO detection kit, Diaminofluorescein-FM diacetate (DAF-FM DA) kit was purchased from Beyotime Biotechnology Co. (Shanghai, China). Matrigel and Transwell plates were purchased from Corning Incorporated (New York, USA). The enzyme-linked immunosorbent assay (ELISA) kit of vascular endothelial growth factor (VEGF) was purchased from ELK Biotechnolog Co. (Wuhan, China). Tumor necrosis factor-α (TNF-α) and interleukin-10 (IL-10) ELISA kites were purchased from Biotechnology Co. (Wuhan, China). Interleukin-6 (IL-6) ELISA kit was purchased from Bioswamp Biotechnology Co. (Wuhan, China). All chemical reagents are purified by any means.

Bacteria Culture, Cell Culture, and Animals: *Escherichia coli* (*E. coli*) and *S. aureus* were acquired from the China General Microbiological Culture Collection Center, and both bacterial strains were cultivated in LB nutrient broth at 37 °C. National Institutes of Health 3T3 (NIH-3T3) and Human umbilical vein endothelial cell (HUVEC) cell lines were obtained from Procell, and were cultured using DMEM medium containing 10% FBS and 1% penicillin-streptomycin at 37 °C with 5% CO_2. The male Sprague−Dawley (SD) rats used *in vivo* experiments were purchased from the Animal Experimental Center of Three Gorges University. The experimental protocol was approved by the Institutional Animal Care and Use Committee of Wuhan University (WP20230010).

2.2. *Preparation and characterization of nanoparticles*

One hundred and forty microliter $Zn(NO_3)_2 \cdot 6H_2O$ solution (0.5 mol/L) dissolved in methanol was added to 2 mL 2-methylimidazole aqueous solution (2.5 mol/L) and then stirred at 1675 g for 30 min at room temperature. The resulting white precipitate was collected by centrifugation at 12,280×g for 30 min and washed three times with ultrapure water to finally obtain ZIF-8 NPs. As to preparing Arg@ZIF-8 NPs, the preparation method was the same as ZIF-8 NPs in addition to the inclusion of L-Arg (20 mg) in the 2-methylimidazole aqueous solution. The NP size was determined using dynamic light scattering (DLS, Malvern, Zetasizer Nano ZSP, Spectris plc., Malvern, UK) and transmission electron microscopy (TEM, Hitachi, HT7700, Hitachi, Ltd., Tokyo, Japan). The NP diffraction peaks were identified by X-ray diffractometer (XRD, Panalytical, XPert Pro, PANalytical B.V., Almelo, Holland), and the characteristic peaks of the NPs were confirmed through Fourier transform infrared spectroscopy (FTIR, Thermofisher, Nicolet iS50, Thermo Fisher Scientific Inc., Waltham, USA). Thermogravimetric analysis (TGA, Mettler-Toledo, TGA2/DSC3, Mettler-Toledo International, Inc., Columbus, USAS) and high throughput surface area and porosity analyzel (N_2 sorption isotherms, Micromeritics, TriStar II 3020, Micromeritics Instrument Corp., Georgia, USA) were also utilized to further demonstrate the successful loading of Arg into the ZIF-8 NPs.

2.3. The pH-responsive release from Arg@ZIF-8 NPs in vitro

First, 5 mg Arg@ZIF-8 NPs were added into 10 mL phosphate-buffered saline (PBS) solution with different pH values (5.6 and 8.0) at 37 °C, respectively. Then, 1 mL supernatant solution was collected at predetermined time points, and 1 mL fresh PBS solution was subsequently added to keep the release medium volume constant. After that, the released Arg was measured by using an amino acid content assay kit, and the Zn^{2+} concentration was measured by inductively coupled plasma mass spectrometry (ICP-MS, Analytikjena, PQ-MS, Analytik Jena AG., Jena, Germany).

2.4. Preparation and characterization of MN patches

The MN patch was prepared with two steps by high-speed centrifugation and vacuum casting methods. First, 1 mg GOx was added to 1 mL of 30% methacrylated gelatin aqueous solution (containing 0.5% photoinitiator) to prepare the first-layer solution. Then, 100 μL of the first-layer solution was placed onto a PDMS mold, followed by centrifugation at 4690×*g* for 5 min to fill the front part of the PDMS mold cavity. To solidify the GelMA gels, the mold was illuminated with ultraviolet (UV) light (365 nm, 100 W) for 3 min. For the fabrication of the second-layer part of MNs, Arg@ZIF-8 NPs were first dispersed in 16% HA aqueous solution to obtain a suspension (15 mg/mL). Then, 100 μL of the suspension was placed on a mold that had already been cast with GOx. After that, the mold was then kept on a vacuum chuck with a vacuum pressure of −0.1 MPa for 2 h, followed by drying in a desiccator at room temperature for 72 h. Finally, the GOx/Arg@ZIF-8 MN (G/AZ-MN) patch could be obtained by demolding.

The bright field images of the MNs were captured by a fluorescence microscope (Olympus, SZX16, Olympus Corporation, Tokyo, Japan). The microstructure of the MNs was captured by the scanning electron microscope (SEM, Hitachi SU8010, Hitachi, Ltd., Tokyo, Japan). The mechanical property of the MNs was determined by a mechanical testing machine (Mark-10, ESM303, Mark-10 Corporation, New York, USA).

2.5. The responsive release of GOx from MN patches

To investigate the responsive release of GOx from MN patches, GOx was used when preparing the MN patch. The MN patch was immersed in a PBS solution at 37 °C with the presence of 50 nmol/L MMP-9. At various time intervals, the supernatant was collected and the release of GOx was quantified using a UV−Visible spectrophotometer (UV−Vis).

2.6. Enzyme activity assay of MNs

Since GOx can catalyze glucose into H_2O_2 and gluconic acid, it usually leads to a decrease in pH level and an increase in H_2O_2 concentration in the microenvironment. To investigate the enzyme activity of G/AZ MN patches, one MN patch was placed into deionized water that contained MMP-9 (50 nmol/L) and various concentrations of glucose. The production of H_2O_2 and pH changes were subsequently detected using an H_2O_2 detection kit and a pH meter at different time intervals, respectively.

2.7. Antibacterial activity of MN patches in vitro

First, the G/AZ MN patch underwent ultraviolet disinfection. Then the MN patch was dissolved in PBS solution with different pH, respectively. After that, the solution was added to an LB nutrient broth medium containing either *S. aureus* or *E. coli* and incubated at 37 °C for 24 h. Finally, the medium was diluted 1000 times and spread onto an agar plate. After incubation, the bacterial colonies were observed using photography to evaluate the antibacterial activity of MN patches.

Live/dead fluorescent staining is also a reliable method for assessing antibacterial property. Bacteria in the logarithmic growth stage were collected and washed with PBS solution three times. Subsequently, the MN patch extraction solution was added, followed by incubation at 37 °C for 4 h. After that, a mixture of SYTO-9 and propidium iodide (PI) was added and incubated for 30 min under in the dark. Finally, the bacterial suspension was carefully applied on a glass slide and the fluorescence was examined using confocal laser scanning microscopy (CLSM, Nikon, A1, Nikon Corporation, Tokyo, Japan). After incubation with the G/AZ MN patches, the morphology of the bacteria was also analyzed to evaluate the antibacterial property of MN patches by a field emission scanning electron microscope (FE-SEM, Carl Zeiss, Zeiss SIGMA, Carl Zeiss AG, Jena, Germany).

2.8. Anti-biofilm activity of MN patch in vitro

To investigate the ability of MN patches to inhibit biofilm formation, the following experimental procedure was conducted. First, a confocal dish was added with 2 mL of *S. aureus* suspension. Subsequently, extracted solutions of MN patches at pH 5.6 or 8.0 were added, respectively, and the plate was incubated at 37 °C for 48 h. The plate was gently washed three times with PBS, and then 1 mL of crystal violet solution was added and incubated for 15 min. The absorbance at 570 nm was measured using an enzyme label (TECAN, M200PRO, Tecan Trading AG, Männedorf, Switzerland) after dissolving the stained biofilm in ethanol. Meanwhile, the biofilms subjected to different treatments were stained using the SYTO-9/PI kit and captured by a CLSM for documentation. Moreover, the prepared biofilms were fixed with 4% paraformaldehyde solution for 15 min. And then they were dehydrated by a concentration gradient of ethanol (30%, 50%, 70%, and 90%) for 15 min each. Finally, the biofilms were coated with gold and observed by FE-SEM.

We also investigated the efficacy of MN patches in clearing mature biofilms. In contrast to the previous method, a volume of 2 mL of *S. aureus* was initially inoculated into a 6-well plate with a coverslip and incubated at 37 °C for 72 h to cultivate mature biofilms. Afterward, the supernatant on the membrane surface was carefully aspirated, and a medium containing different types of MNs was introduced for 24 h incubation. Finally, the disruption of the biofilm was assessed by crystalline violet staining, live/dead bacterial staining, and FE-SEM, respectively.

2.9. Biosafety and biocompatibility test of MN patches in vitro

The NIH-3T3 cell line was utilized for evaluating cell viability. The toxicity of the biological materials used in MN patches was assessed by the MTT kit and calcein-AM/PI staining. Each experiment was replicated five times.

To further assess the biocompatibility of MN patches and NPs, rat blood was obtained by anticoagulation tubes. The blood

samples were centrifuged at 1500 rpm for 15 min at 4 °C, and the red blood cells (RBCs) were collected and dispersed in a PBS solution. Two hundred microliter RBCs were mixed with PBS solution containing the MN patch. As negative and positive controls, PBS solution and ultrapure water were used, respectively. The cell suspensions underwent incubation at room temperature for 4 h, followed by centrifugation at 3000 rpm for 10 min. The absorbance of the supernatant at 540 nm was measured by a UV spectrophotometer, and the hemolysis rate was calculated.

2.10. Cell proliferation and migration experiment

MNs extraction was utilized to assess the pro-proliferative and migratory capabilities. NIH-3T3 cells were inoculated in 6-well plates and cultured until reaching confluence after 24 h. A scratch was made on the cell layers by a 200 μL pipette tip. Subsequently, the wells were supplemented with DMEM medium containing different MN extracts. The cells were incubated for 24 h to facilitate the observation of scratch closure. In addition, Transwell assays were used to assess the effect of microtargeting on cell migration. The cell suspension was inoculated into the upper chamber (serum-free medium). However, in the basolateral Transwell chamber, the DMEM medium supplemented with 20% FBS and MN extraction solution was added. Following a 24 h incubation period, non-migrated cells were gently removed from the upper surface by a cotton swab. The migratory cells were then stained with crystal violet and visualized using a fluorescent inverted microscope (Olympus VS200, Olympus Corporation, Tokyo, Japan).

2.11. Intracellular NO generation assay

The presence of NO in HUVEC cells was visualized by employing the fluorescent probe DAF-FM DA. Briefly, HUVEC cells were incubated with DMEM (containing 100 μmol/L H_2O_2) at 37 °C for 12 h. The medium was subsequently aspirated, and the DMEM containing ZIF-8 NPs or Arg@ZIF-8 NPs was introduced. Following incubation for 6 h, DAF-FM DA was applied and incubated for 30 min. CLSM was employed for monitoring cell fluorescence.

2.12. Tube formation assay

The effectiveness of promoting angiogenesis was confirmed through an *in vitro* HUVEC tube-formation assay. Matrigel was melted at 4 °C, and then added to pre-cooled 48-well plates, followed by incubation at 37 °C for 30 min. After the Matrigel completely solidified, HUVEC cell suspension and MNs extraction were sequentially added to the 48-well plates. Then, the HUVEC cells were labeled with calcein after 6 h. Photographs were taken using a fluorescent inverted microscope. The tube length or nodes were measured using Angio Tool software.

2.13. M2 polarization of macrophages

RAW 264.7 macrophages were added to DMEM containing MNs extraction, and cultured for 24 h, where lipopolysaccharide (LPS) was used as a control group. RAW 264.7 cells were collected and stained with CD86, and CD206, and the cells were analyzed by flow cytometry. The levels of IL-6, TNF-α, and IL-10 in cell culture supernatants were analyzed by ELISA kits.

2.14. Establishment of diabetic infected or non-infected wound model and application of MN patches in vivo

All animal care and experimental procedures were approved by the Institutional Animal Care and Use Committee of Wuhan University. Male SD rats (6−8 weeks old, ∼200 g) were obtained from Beijing Vital River Laboratory Animal Technology Co., Ltd. The diabetic models were established by intraperitoneal injection of 2% streptozotocin (STZ). After two weeks, if the blood glucose levels consistently remained above 16.7 mmol/L and exhibited symptoms of polyphagia and polyuria, the rats were considered to have developed diabetes. A full-layered, 10 mm diameter circular wound was created with anesthetized and debrided rat dorsal skin by a biopsy perforator. To establish the diabetic wound infection model, a dropwise addition of 10^7 CFU *S. aureus* (10^9 CFU/mL) was administered to the created wound. After a two-day interval, the diabetic rat infection model was successfully established. Then, MN patches were applied to the wound localization. On Days 3, 6, 9, and 15, photographs of the wounds were taken, and their respective areas were measured. The wound area was further analyzed utilizing ImageJ.

2.15. Skin irritation from MN patches

The MN patch was applied to SD rats. Before insertion, the fur on the back of the SD rats was shaved by an electric shaver, and the exposed skin was disinfected with 75% alcohol and allowed to dry. After attaching the MN patch for 5 min, the changes in the rat's skin at 0, 5, 15, and 30 min were captured using a stereo microscope. Additionally, the skin treated with the MN patch was removed at 0 min, 60 min, and 24 h, and the inflammatory condition of the skin was determined through hematoxylin and eosin (H&E) staining.

2.16. Histological analysis

The wound tissue was fixed in 4% paraformaldehyde for 48 h, and the fixed tissue was then embedded in paraffin and sliced into sections with 5-μm thickness. H&E staining was conducted to observe the width of the granulation tissue, and immune histochemistry (TNF-α) was employed to examine the level of wound inflammation. Additionally, Masson staining was utilized to quantify collagen deposition. For immunofluorescence analysis, the sections were first de-paraffinized, followed by antigen retrieval and sealing. Subsequently, the sections were incubated with primary antibodies, specifically rabbit monoclonal anti-CD31 and rat monoclonal antibody α-SMA. Afterward, the sections were co-incubated with corresponding secondary antibodies, and the nuclei were stained by DAPI. Finally, ImageJ was utilized to quantify the staining results.

2.17. In vivo biosafety assessment

To assess the biosafety of MNs, blood samples were collected from rats on Day 7 after treatment for further analysis. Moreover, major organs of the rats, including the heart, liver, spleen, lung, and kidney, were collected on Day 15 for H&E staining. All

histological sections were recorded using a fluorescent inverted microscope.

2.18. Statistical analysis

Statistical analysis was performed with the aid of Origin software, Angio Tool software, and ImageJ software. All data are expressed as mean ± standard deviation, and at least 3 samples per experiment were used for statistical analysis of the data. Statistical analyses were performed by one-way analysis of variance (ANOVA) and Student's *t*-test, and $P < 0.05$ was considered statistically significant ($^{*}P < 0.05$, $^{**}P < 0.01$, $^{***}P < 0.001$, $^{****}P < 0.0001$).

3. Results

3.1. Synthesis and characterization of Arg@ZIF-8 NPs

The Arg@ZIF-8 NPs were synthesized by using the *in situ* loading method, incorporating zinc nitrate, 2-methylimidazole, and Arg as primary constituents. The XRD result revealed that the diffraction peak of the synthesized Arg@ZIF-8 NPs was similar to that of ZIF-8 NPs, indicating the Arg@ZIF-8 NPs maintained the identical crystal structure and crystallinity as the ZIF-8 NPs (Fig. 2A). According to DLS analysis (Fig. 2B), the formed NPs featured an average hydrodynamic diameter of 158.2 ± 9.5 nm and a narrow size distribution. The FTIR spectrum of Arg@ZIF-8 NPs, as shown in Fig. 2C, exhibited an absorption peak at 1615 cm^{-1}, which was assigned to the amino acid of Arg, suggesting that Arg was successfully encapsulated in the ZIF-8 NPs. To provide additional evidence for the existence of Arg, the NPs were analyzed by UV−Vis. As shown in Supporting Information Fig. S1, a characteristic absorption peak of Arg was detected at a wavelength of 570 nm using the ninhydrin method, demonstrating successful encapsulation of the amino acid in ZIF-8 NPs. TGA analysis and N_2 adsorption−desorption further confirmed the incorporation of Arg inside ZIF-8 NPs (Fig. 2D and E). Moreover, the drug loading efficiency (LE) and encapsulation efficiency (EE) of Arg in NPs were determined as 26.7 ± 1.2% and 83.9 ± 4.4%, respectively, which was analyzed through UV−Vis absorption spectroscopy (Supporting Information Fig. S2).

After the synthesis of Arg@ZIF-8 NPs, their acid-responsive property was next examined by XRD analysis (Fig. 2F) and TEM (Fig. 2H), which showed that Arg@ZIF-8 NPs maintained their original crystal structure and crystallinity at pH 8.0, but showed structural dissociation at pH 5.6. Additionally, DLS measurement was further conducted to investigate the behavior of Arg@ZIF-8 NPs under acidic conditions. As shown in Fig. 2G, the polydispersity index (PDI) of NPs significantly increased when placed in the acid environment, suggesting a deterioration in the dispersion of the Arg@ZIF-8 NPs, which was primarily ascribed to the dissociation of the NPs structure. This pH-responsive characteristic greatly facilitated the release of Arg from Arg@ZIF-8 NPs in acidic environments. As shown in Fig. 2I, in a weakly alkaline condition (pH 8.0), which mimicked a diabetic wound microenvironment, there was only little Arg released from ZIF-8 NPs. However, when the environment became acidic (pH 5.6), the NPs exhibited robust release of the amino acid (*i.e.*, Arg) within 24 h, demonstrating the pH-responsive release of the Arg from ZIF-8 NPs.

3.2. Fabrication and characterization of the G/AZ-MN patches

To achieve minimally invasive and highly efficient drug delivery in wound beds, we designed a microenvironment-responsive bilayer MN patch (G/AZ−MN patch) through a sequential casting method. The first layer of MN was prepared using a blend of GelMA that possesses sensitivity to MMP-9, along with GOx, and the second layer of MN was made by using a combination of HA with low molecular weight and Arg@ZIF-8 NPs (Supporting Information Fig. S3). The resulting patch contained a 10 × 10 MNs array arranged in an area of ∼0.5 cm^2. Each MN exhibited a sharp cone structure, with 850 μm in height and 400 μm in base diameter (Fig. 3A). The mechanical strength of G/AZ-MNs was evaluated using a mechanical tester, which determined that it possessed a strength of approximately 0.7 N per needle (Supporting Information Fig. S4A). The MN tips showed rapid separation from the patch after the dissolution of the base layer, as evidenced by the real-time record of the MN patch in PBS solution (Supporting Information Fig. S5, Supporting Information Video S1). To assess the ability of the MNs to penetrate the skin, the MN patch was further applied to porcine skin *ex vivo*. The double layers of MN encapsulated two kinds of fluorescent dyes for better visualization (FITC-BSA in the tip layer, and RB@ZIF-8 NPs in the base layer) (Fig. 3C). As shown in Fig. 3B and C, MNs could successfully deliver both two fluorescent dyes into the skin, leaving little dye in the residual patch, which was further confirmed by histological sections of the porcine skin (Fig. S4B). Wiping the punctured porcine skin also validated that the MNs penetrated into the skin and did not break on the skin surface (Supporting Information Fig. S6). It was determined that drugs loaded in the MN patch were 10.5 ± 2.4 μg in the tip layer and 281.9 ± 5.9 μg in the base layer, and these drugs could be delivered in the skin with the amount of 10.3 ± 2.2 μg and 246.5 ± 2.1 μg, respectively, both achieving about 90% delivery efficiency in the skin (Fig. S4C). Additionally, the enzyme of GOx showed great stability in the tip layer for over 14 days (Supporting Information Fig. S7).

Supplementary video related to this article can be found at https://doi.org/10.1016/j.apsb.2024.06.014

It has been reported that the enzyme of MMP-9 was found to be overexpressed in diabetic wounds, exhibiting a 14-fold increase compared to normal tissue wounds[25]. As the first layer of G/AZ-MNs was composed of GelMA that can degrade over time after exposure to MMP-9, incubation G/AZ-MNs with PBS solution containing 50 nmol/L MMP-9 resulted in sustained release of the encapsulated GOx for over 144 h (*i.e.*, 6 days) (Fig. 3D). Subsequently, the released GOx catalyzed glucose, producing H_2O_2 and gluconic acid during the oxidation reaction, which caused an increase of H_2O_2 and decrease of pH value in the environment (Fig. 3E and F). The reduced pH value could trigger the degradation of Arg@ZIF-8 NPs and cause subsequent release of Arg. To further demonstrate the properties of MMP-9 responsive degradation and pH-responsive release, MNs that contained FITC-BSA in the tip layer or RB@ZIF-8 NPs in the base layer were inserted into four kinds of agar gels (with or without MMP-9, pH 8.0 or 5.6). It was observed that the fluorescence of MNs faded more rapidly after insertion into the gel with MMP-9 due to the degradation of the GelMA layer (Fig. 3G and H). When inserting MNs into the gel with pH 5.6, the red fluorescence dye diffused more deeply than the gel with pH 8.0, which was mostly attributed to the degradation of RB@ZIF-8 NPs under the acidic condition,

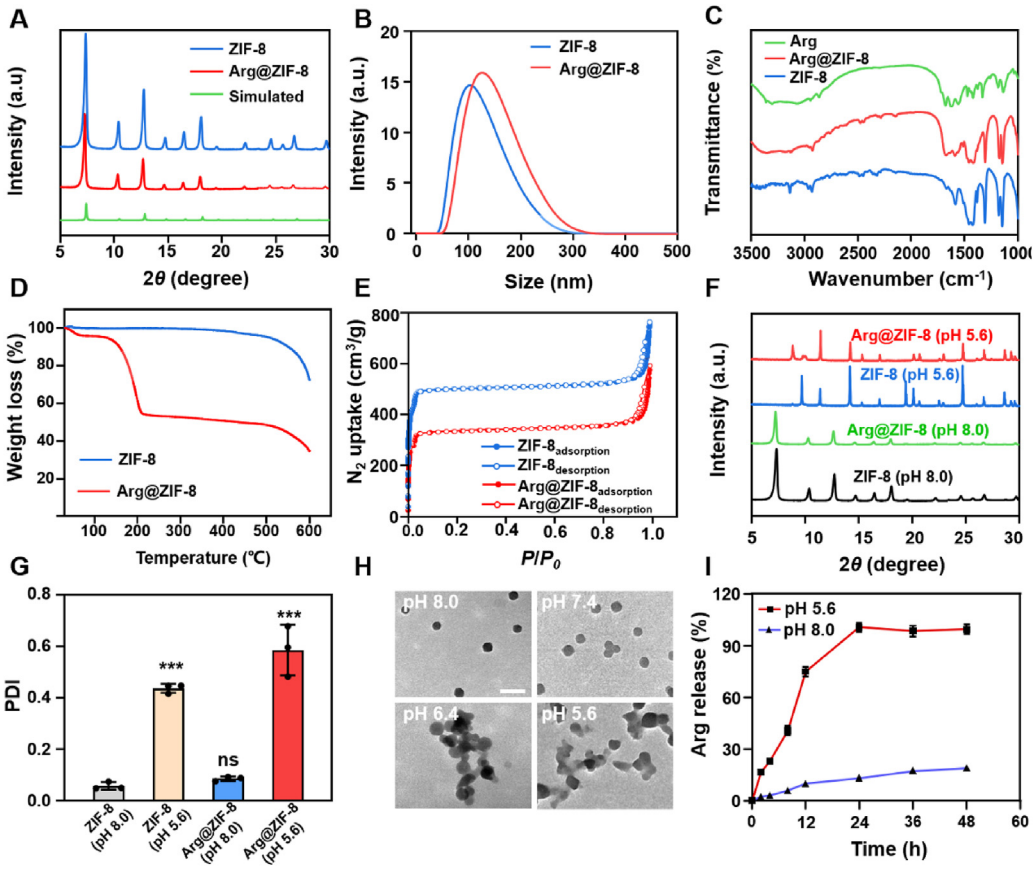

Figure 2 Synthesis and characterization of Arg@ZIF-8 NPs. (A) XRD of ZIF-8 NPs and Arg@ZIF-8 NPs. (B) Dynamic light scattering (DLS) of ZIF-8 NPs and Arg@ZIF-8 NPs. (C) FTIR spectra of Arg, ZIF-8 NPs and Arg@ZIF-8 NPs, respectively. (D) TGA curves of ZIF-8 NPs and Arg@ZIF-8 NPs. (E) The nitrogen absorption curve of ZIF-8 NPs and Arg@ZIF-8 NPs. (F) XRD of ZIF-8 NPs and Arg@ZIF-8 NPs at different pH environments (pH 5.6 or pH 8.0). (G) The polydispersity index (PDI) variation of ZIF-8 NPs and Arg@ZIF-8 NPs under different pH conditions (pH 5.6 or pH 8.0). (H) TEM images of Arg@ZIF-8 NPs treated by different pH buffers. Scale bar: 200 nm. (I) Drug release profile of Arg from Arg@ZIF-8 NPs under different releasing media ($n = 3$ independent samples, $^{*}P < 0.05$, $^{**}P < 0.01$, $^{***}P < 0.001$, $^{****}P < 0.0001$).

leading to the release of RB from NPs and subsequent diffusion into the deep side of the gel (Fig. 3I and J). Moreover, we determined that the prepared G/AZ-MNs possessed satisfactory biocompatibility *in vitro* by cytotoxicity assay, live/dead cell staining, and hemolysis test (Supporting Information Fig. S8).

3.3. Antibacterial and anti-biofilm activities of G/AZ-MN patches in vitro

We next investigated the antibacterial and anti-biofilm activities of G/AZ-MN patches *in vitro*. After being placed in the PBS medium with pH 5.6, MN patches generated robust Zn^{2+} due to the degradation of ZIF-8 NPs at the acidic condition (Fig. 4A), which exhibited satisfactory antibacterial activity for *E. coli* and *S. aureus* (Fig. 4B and Fig. S6A and S6B). Such excellent capability of G/AZ-MN patches to inhibit bacterial growth at acidic conditions was further confirmed by the live/dead bacterial staining (Fig. 4C and D, Supporting Information Figs. S9 and S10) and FE-SEM which showed that bacterial membrane exhibited wrinkled and rough surfaces with severe damage after incubation with G/AZ-MN patches at pH 5.6 for 6 h (Fig. 4E). Collectively, these results demonstrated the exceptional bactericidal effect of G/AZ-MN patches.

The presence of bacterial biofilm in chronic wounds poses a significant challenge for treatment efficacy[8,26], since the biofilm creates a protective barrier that prevents the penetration of topically applied antibacterial drugs[27]. Therefore, we further examined the capability of the designed bilayer MN patch to inhibit biofilm formation. It was found that the treatment with G/AZ-MNs at pH 5.6 could not only inhibit the formation of immature biofilms (Fig. 4F and H), but also disrupt and eradicate the already formed mature biofilms (Fig. 4G and I). Quantitatively, G/AZ-MNs at alkaline conditions showed less than 10% inhibition efficiency of immature biofilm or clearance efficiency of mature biofilm, while exhibiting over 80% efficiency either for immature biofilm inhibition or for mature biofilm destruction at acidic conditions (Fig. 4J and K), indicating a great anti-biofilm activity of the G/AZ-MN patches.

3.4. Glucose depletion and sustained release of NO from G/AZ-MNs for angiogenesis and cell migration promotion in vitro

To assess the capacity of G/AZ-MNs for long-term release of NO, the Griess kit assay was used to measure the produced NO in the release medium, which revealed that G/AZ-MNs could achieve sustained release of NO for about 7 days (*i.e.* 168 h) (Fig. 5A).

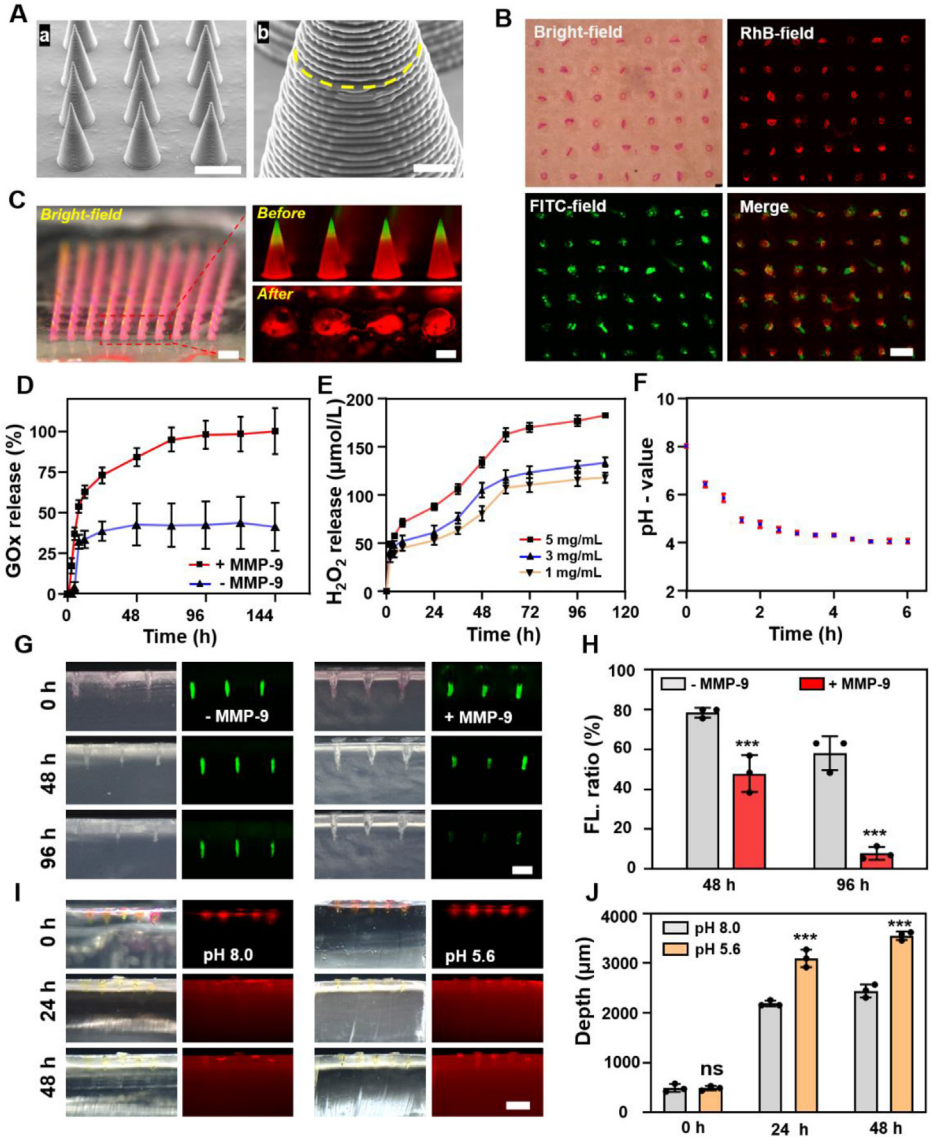

Figure 3 Fabrication and characterization of the MN patch. (A) SEM images of G/AZ-MN patch. Scale bar, 500 μm in (a); Scale bar, 200 μm in (b). The yellow line indicated the connection between the MN-tip layer and MN-base layer. (B) Representative images of bright-field and fluorescence-field of pig skin after being punctured by the MN patch. Scale bar, 750 μm. (C) Left: optical image of the bilayer MNs (Scale bar, 1 mm). Right: fluorescent images of MNs before and after insertion into pig skin *ex vivo*. Scale bar, 250 μm. (D) Accumulated release of GOx from MN-tip layer in PBS with or without MMP-9. (E) Cumulative production of H_2O_2 after placing the MN-tip layer in PBS with different glucose concentrations. (F) The measurement of pH value at different time points in the MN-tip catalyzing glucose reaction system. (G) Degradation of MN tips containing FITC-BSA in agarose gels (simulated skin) with or without MMP-9 at different time points. Scale bar, 250 μm. (H) Quantitative analysis of the fluorescence intensity in (G). (I) The diffusion of RB@ZIF-8 NPs released from MN-base layer in agarose gels with different pH values at different time points. Scale bar, 1 mm. (J) Quantitative analysis of diffusion depth in (I). $n = 3$ independent samples, $^{*}P < 0.05$, $^{**}P < 0.01$, $^{***}P < 0.001$, $^{****}P < 0.0001$.

The application of NO fluorescent probe DAF-FM DA also validated the sufficient generation of NO in HUVEC cells after incubation with G/AZ-MNs and H_2O_2 (Supporting Information Fig. S11A). It has been reported that exogenous NO can effectively promote the healing of diabetic wounds[19,28,29]. Therefore, the potential of G/AZ-MNs in promoting fibroblast migration was next evaluated through the scratch test and Transwell assay, which indicated a significantly higher scratch closure and enhanced migration rate in the treatment of G/AZ-MNs compared to other treatments (Fig. 5B and Fig. S11B, S11C and S11J). Cell migration was also promoted in the G/Z-MNs group in comparison to the control group, potentially due to the release of Zn^{2+} from G/Z-MNs that has been reported to induce fibroblast proliferation and migration[30].

In diabetic wound healing, vascular dysfunction that generally results from prolonged hyperglycemia is a primary factor contributing to treatment failure[31,32]. It was found that the developed G/AZ-MN patch displayed good capability of reducing glucose concentration during incubation with HUVEC cells at a high glucose level (33 mmol/L) that simulated the

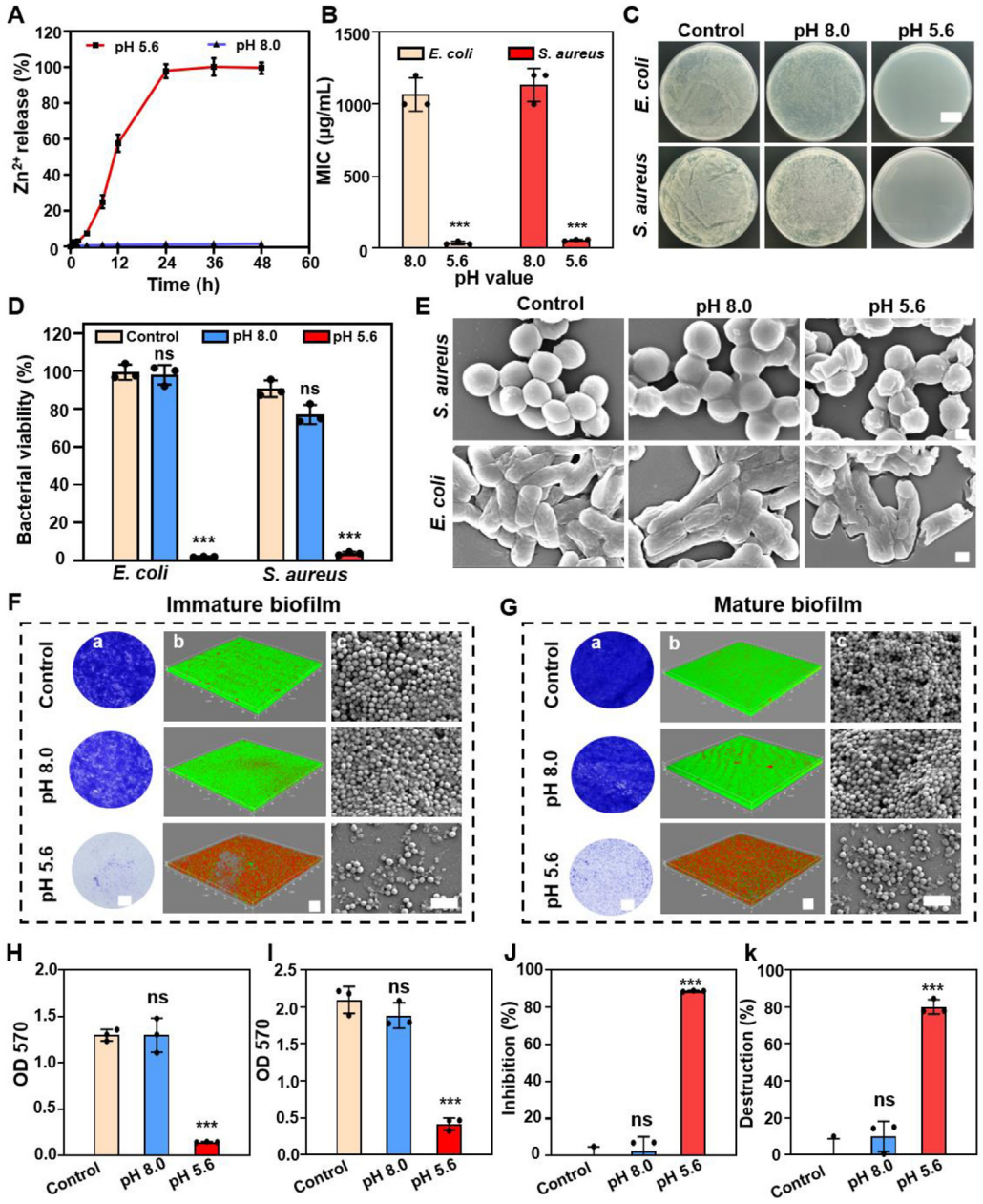

Figure 4 Antibacterial activity of NPs and MNs. (A) Accumulated release of Zn^{2+} from G/AZ-MN patches. (B) Minimum inhibitory concentration of Arg@ZIF-8 NPs in G/AZ-MNs against *E. coli* or *S. aureus*. (C) Photographs of agar plates showing the antibacterial activity of G/AZ-MNs against *E. coli* and *S. aureus*. Scale bar, 20 mm. (D) Bacterial viability of *E. coli* and *S. aureus* after receiving the treatment of G/AZ-MNs at different pH values. (E) FE-SEM images of morphology changes of *E. coli* and *S. aureus* after the treatment with G/AZ-MNs at different pH values. Scale bar, 400 nm. (F) The inhibitory effect of G/AZ-MNs against *S. aureus* biofilm. (a) Photographs of the immature biofilms stained by crystal violet. Scale bar, 50 μm. (b) Confocal images and corresponding 3D images of SYTO/PI-stained immature biofilms after different treatments. Scale bar, 200 μm. (c) The FE-SEM images of immature biofilms with different treatments. Scale bar, 25 μm. (G) The destruction effect of G/AZ-MNs against *S. aureus* biofilm. (a) Photographs of the mature biofilms stained by crystal violet. Scale bar, 50 μm. (b) Confocal images and corresponding 3D images of SYTO/PI-stained mature biofilms after different treatments. Scale bar, 200 μm. (c) The FE-SEM images of mature biofilms with different treatments. Scale bar, 25 μm. (H) Corresponding optical density (OD) 570 value of immature biofilms of each group. (I) Corresponding OD 570 value of mature biofilms of each group. (J) The inhibition rate of immature biofilms. (K) The destruction rate of mature biofilms. $n = 3$ independent samples, $^{*}P < 0.05$, $^{**}P < 0.01$, $^{***}P < 0.001$, $^{****}P < 0.0001$.

microenvironment of diabetic wounds (Fig. 5C). Furthermore, such treatment with the G/AZ-MN patch significantly improved the cell survival rate and proliferation rate compared to other control groups, as demonstrated by MTT assay and calcein staining (Fig. S11D and S11E) which was mostly ascribed to glucose level reduction in the culture medium enabled by GOx.

To determine the effect of G/AZ-MN patches on the revascularization of diabetic wounds, HUVEC cells were cultured in a

medium containing high-concentration glucose (33 mmol/L), followed by incubation with the G/AZ-MN patch. As shown in Fig. 5D and Fig. S11F, the presence of G/AZ-MNs led to stronger green fluorescence, characterized by the formation of longer and more branching tubes by HUVEC cells (Fig. 5D and Fig. S11F). Additionally, the application of G/AZ-MNs exhibited an obvious increase in the expression of angiogenic growth factors (*e.g.*, VEGF) in HUVEC cells (Fig. 5E, Fig. S11G and S11H), which was extremely important for promoting blood vessel growth and revascularization in diabetic wounds.

Collectively, these results indicated that the designed G/AZ-MN patch could reduce glucose levels by the delivery of GOx and promote cell migration and VEGF-mediated revascularization through sustained release of NO *in vitro*.

3.5. Anti-inflammatory property of G/AZ-MN patches

The process of wound healing is greatly associated with the crucial polarization of macrophages into either pro-inflammatory (M1 phenotype) or anti-inflammatory (M2 phenotype) phenotypes[33]. Remarkably, it has been demonstrated that NO plays a role in facilitating the transformation of M1 macrophages into M2 macrophages[28]. Through comprehensive analysis using immunostaining and flow cytometry techniques, we observed that G/AZ-MNs effectively facilitated the transformation of LPS-stimulated M1 macrophages into M2 macrophages, as evidenced by an augmented expression of CD206 and a reduced expression of CD86 (Fig. 5F, G and Fig. S11I). Furthermore, the use of G/AZ-MNs significantly down-regulated the expression of pro-inflammatory factors, IL-6 (Fig. 5H) and TNF-α (Fig. 5I), while up-regulating the level of the anti-inflammatory cytokine IL-10 (Fig. 5J). Together, these findings suggested the anti-inflammatory property of G/AZ-MN patches.

3.6. Wound healing promotion by G/AZ-MN patches in diabetic wounds in vivo

The diabetic rat model was established *via* intraperitoneal injection of 2% STZ (Fig. 6F). After that, full-thickness wounds were created on the dorsal region of diabetic rats through the puncturing of the skin. The rats were then randomly divided into five groups, receiving: (1) no treatment (*i.e.*, control group), (2) BL-MNs group (*i.e.*, blank MNs composed of Gel-MA and HA), (3) Z-MNs group (*i.e.* MNs containing only ZIF-8 NPs), (4) G/Z-MNs group (*i.e.*, MNs containing GOx and ZIF-8 NPs), and (5) G/AZ-MNs group (*i.e.*, MNs containing GOx and Arg@ZIF-8 NPs). As shown in Fig. 6A, B, and 6G, the rats that were treated with G/AZ-MNs exhibited the most rapid healing rate compared to rats in other groups, which was further validated by histologic analysis, including H&E staining (Fig. 6C), Masson staining (Fig. 6D), as well as immunofluorescence staining for CD31 and VEGF (Fig. 6E). In the G/AZ-MNs group, Masson staining result displayed the highest collagen volume fraction (CVF) (Fig. 6H), and CD31/VEGF immunofluorescence staining result showed the strongest fluorescence intensity (Fig. 6I), indicating the best therapeutic result after the treatment of G/AZ-MNs in diabetic wounds *in vivo*. Therefore, these findings demonstrated the superior capability of G/AZ-MNs to facilitate diabetic wound regeneration. Furthermore, we assessed the pH value change at the wound before and after MNs application. As shown in Supporting Information Fig. S12, the wound tissue exhibited an alkali pH value (8.1 $\pm$ 0.3) before therapy, which was consistent with the literature report[34,35]. However, the pH value at the wound lesion shifted to 5.7 $\pm$ 0.2 two days post treatment with G/AZ MNs, due to the oxidation of glucose and generation of gluconic acid, thereby being able to trigger the dissociation of pH-responsive NPs and cause drug release from the NPs.

3.7. Wound healing promotion by G/AZ-MN patches in infected diabetic wounds in vivo

Owing to the localized hyperglycemic microenvironment at diabetic wounds, pathogenic bacteria are very likely to colonize at wounds and generate bacterial biofilms, thereby forming infectious diabetic wounds, which always delays the healing process at wounds[32,36]. Therefore, we further investigated whether the designed bilayer G/AZ MN patch still possessed the function of accelerating infected wound closure in diabetic rats. As indicated in Fig. 7A, infected diabetic wounds were developed by inoculation of *S. aureus* after the creation of wounds in the diabetic rat model. After that, the rats were randomly divided into six groups: (1) control group (receiving no treatment), (2) BL-MNs group (receiving blank MNs), (3) Z-MNs group (receiving MNs only containing ZIF-8 NPs in the base layer), (4) EM group (applied topically), (5) G/Z-MNs group (receiving MNs that contained GOx in the tip layer and ZIF-8 NPs in the base layer), and (6) G/AZ-MNs group (receiving MNs that contained GOx in the tip layer and Arg@ZIF-8 NPs in the base layer). After the treatment, the wounds were photographed and measured on Days 0, 3, 6, 9, 12, and 15. As shown in Fig. 7B, wounds treated with G/AZ-MNs exhibited a fast closure rate, and the G/AZ-MNs group displayed a wound healing rate of 98.2 $\pm$ 1.3% on Day 15, which was significantly higher than other groups (Fig. 7H). To assess the anti-biofilm property of G/AZ-MNs, bacteria at the wound bed were collected from the five groups and subsequently cultured on agar plates on Day 3. It was observed that both the G/AZ-MNs and G/Z-MNs groups displayed the least bacterial colonies and lowest bacterial survival rate compared to other groups (Fig. 7F and G), which could attribute to the degradation of the encapsulated ZIF-8 NPs and subsequent release of Zn^{2+}, thereby achieving effective removal of the bacterial biofilm.

We conducted a histological analysis to obtain a more detailed understanding of the wound-healing process. We utilized H&E staining to investigate the contraction of the wound bed and the progress of epithelialization. Although tissue defects from all groups were observed on Day 3 (Supporting Information Fig. S13), the wounds treated with G/AZ-MNs showed the smallest width compared to other groups on Day 6 (Fig. 7D and I). Immunohistochemical experiments indicated a decrease in TNF-α expression in the wounds (Fig. 7E and J) after receiving the treatment of G/AZ-MNs, suggesting that the G/AZ-MNs had an efficient anti-inflammatory effect on the wound bed. The routine blood analysis demonstrated a decrease in various immune cells, including white blood cells, lymphocytes, and granulocytes after the treatment with G/AZ-MNs (Supporting Information Fig. S14), which was consistent with the result of TNF-α expression, further demonstrating the anti-inflammation property of G/AZ-MNs.

High blood glucose levels around the wound have been found to significantly delay wound healing. Hence, we conducted periodic acid-Schiff (PAS) staining to evaluate the glucose change after treatment of G/AZ-MNs. As shown in Fig. 7C and Fig. S13B, either the control or BL-MNs or Z-MNs group exhibited an apparent purple-red color, indicating a high blood glucose level in the wound areas. In contrast, the treatment with G/Z-MNs or

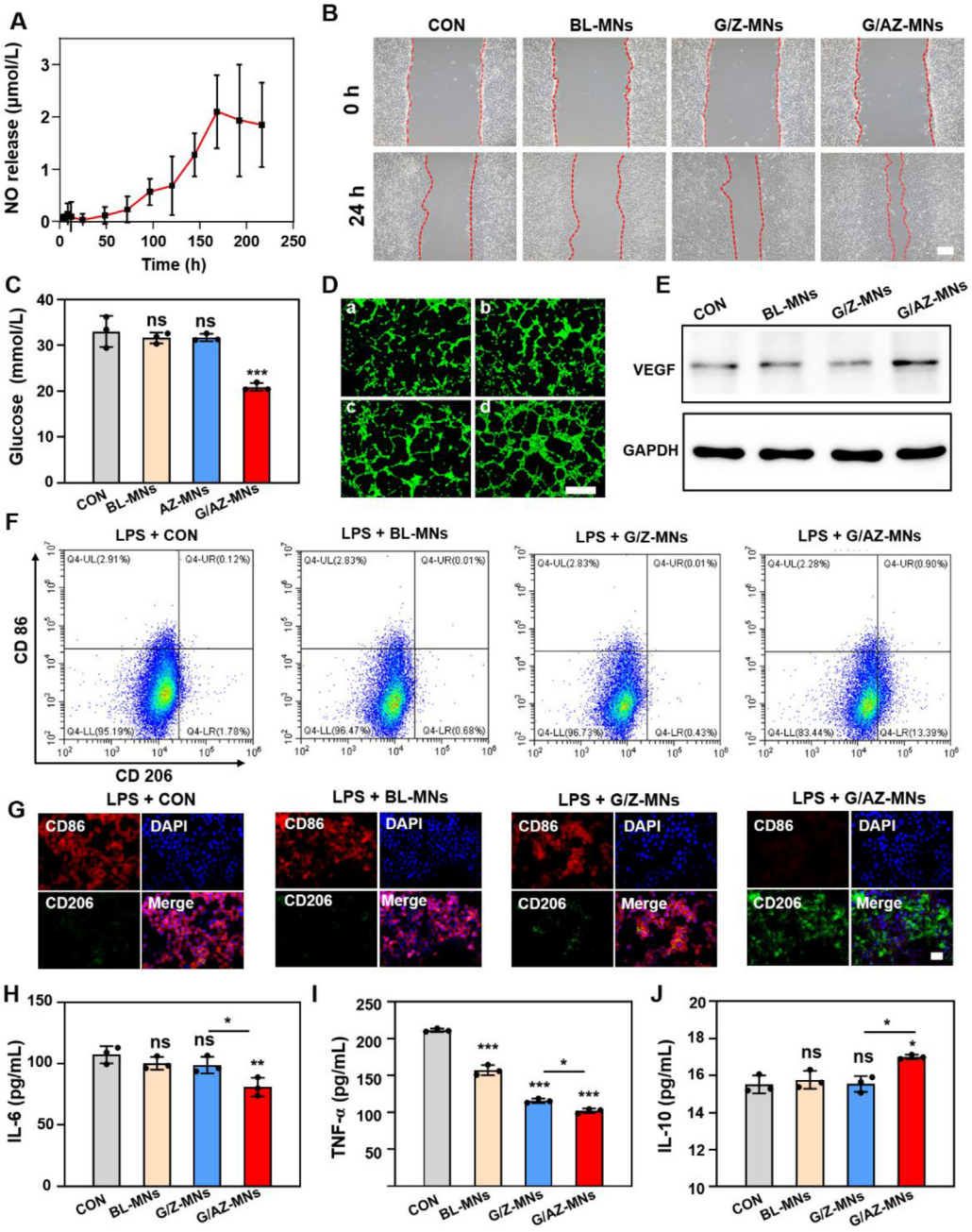

Figure 5 Evaluation of cell migration, angiogenesis, and macrophage polarization after the treatment of G/AZ MNs. (A) The *in vitro* release of NO from G/AZ-MNs in PBS buffer containing MMP-9 and glucose. (B) Representative photographs of NIH-3T3 cells scratches at 0 and 24 h co-cultured with different MNs. Scale bar, 200 μm. (C) Glucose concentration of supernatants after incubating HVUEC cells with different MNs medium for 24 h, respectively. (D) Confocal images of vascular tube-formation with HUVEC cells co-cultured with different MNs. Scale bar, 100 μm. (E) Protein expression levels of VEGF in HUVEC cells after being treated with different MNs as determined by Western-Blot. (F) Representative flow cytometry plots of macrophage cells. (G) Representative images of the M1/M2 levels in the different groups. Scale bar, 50 μm. (H–J) Expression of IL-6 (H), TNF-α (I), and IL-10 (J) in RAW264.7 cells induced by lipopolysaccharides (LPS) in the different groups. $n = 3$ independent samples, $^{*}P < 0.05$, $^{**}P < 0.01$, $^{***}P < 0.001$, $^{****}P < 0.0001$.

G/AZ-MNs showed a much lighter purple-red color, suggesting that G/A-MNs or G/AZ-MNs could effectively reduce glucose concentration in the local wound area.

In addition, the complete epidermis and multiple skin sublayers were observed in wounds treated with G/AZ-MN patch 15 days post-treatment, while other groups still exhibited severe tissue defects (Fig. 8A and D). Masson staining confirmed the regular arrangement of collagen and a higher volume fraction in the G/AZ-MNs group, indicating its ability to promote extracellular matrix deposition (Fig. 8B and E). Angiogenesis is a key factor in effective wound healing, and sparse vessel formation was observed in the control, BL-MNs, Z-MNs, or G/Z-MNs group, suggesting reduced vascularization in these groups (Fig. 8C). However, the G/AZ-MNs group, which was able to continuously

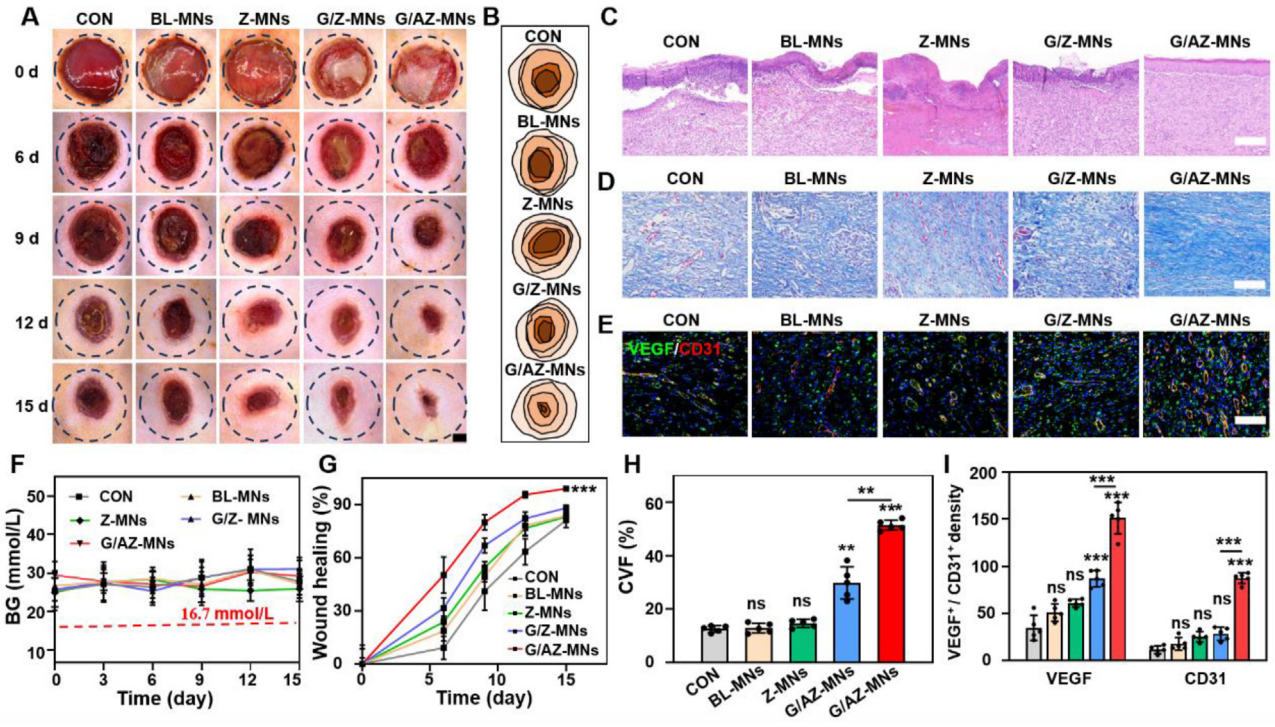

Figure 6 G/AZ-MNs promoting noninfectious diabetic wound healing. (A) Representative photographs of wounds in SD rats at different time points after different treatments. Scale bar, 2 mm. (B) Simulated images of wound healing in noninfected diabetes wounds. Representative H&E (C) or Masson staining (D) or immunofluorescence images of CD31-positive (red) and VEGF-positive (green) (E) of wound tissues in different groups on Day 15. Scale bars, 100 μm. (F) Blood glucose (BG) concentrations in diabetic rats during treatment. (G) Quantitative analysis of noninfected diabetes wound healing rate in different groups. (H) Quantitative analysis of collagen volume fraction (CVF) in different groups. (I) Quantification of $CD31^+$ density and $VEGF^+$ density. $n = 5$ independent samples, $^*P < 0.05$, $^{**}P < 0.01$, $^{***}P < 0.001$, $^{****}P < 0.0001$.

release NO in the wounds, exhibited significantly increased blood vessel density (CD31 staining), with an average microvessel density of 139.8 ± 13.0 (Fig. 8F). The immunostaining for α-SMA exhibited a similar pattern to CD31 staining (Fig. 8G), further demonstrating the therapeutic angiogenesis capability of G/AZ-MNs *in vivo*.

Finally, we assessed the biosafety and biocompatibility of G/AZ-MNs in animals. Application of the MNs in rats created an array of microporous holes in the applied skin initially, but these holes were fully closed within 15 min without causing any obvious inflammation (Supporting Information Fig. S15). The blood biochemical analysis (Supporting Information Fig. S16) and H&E staining of major organs (heart, liver, spleen, lungs, and kidneys) on Day 15 (Supporting Information Fig. S17) further confirmed the biosafety of G/AZ-MNs *in vivo*.

4. Discussion

In diabetic patients, localized hyperglycemia around the wound disrupts the normal functioning of signaling pathways and biological factors involved in angiogenesis[37,38]. This impaired function also affects angiogenic cells, reducing their ability to proliferate, migrate, and form blood vessels[39]. Besides, bacterial infection and unresolved inflammation are two other reasons that cause difficulty in diabetic wound healing. Furthermore, once infected, the bacteria are very likely to form a biofilm on the wound, which acts as a barrier to prevent the delivery of therapeutic drugs, thereby significantly reducing the therapeutic efficacy of the drug in killing the deleterious bacteria[26,40]. Recently, scientists have made notable advancements in identifying various facilitating agents and mechanisms that promote the healing of chronic wounds. For example, Ge et al.[17] reported a kind of microenvironment-responsive self-delivery GOx@manganese sulfide (GOx@MnS) NPs for diabetic wound treatment *via* the reduction of glucose levels and antibacterial and anti-inflammatory effects through the release of manganese ions and hydrogen sulfide. However, the therapeutic efficacy of the system in adjusting the hyperglycemic condition and eliminating the malignant bacteria that are located in the biofilms might be compromised, due to the topical application approach and difficulty of the NPs in penetrating in the bacterial biofilms. Recently, MN patches have been adopted for chronic wound therapy with improved drug delivery efficiency by physically crossing the barrier of biofilms[41,42], while these MN patches usually suffer from mono-therapy or short-acting effect. There are also other facilitators to promote wound healing, which encompass hydrogen (H_2)[16,43], oxygen (O_2)[44-47], and NO[48-50]. Of particular interest is the role of NO, a gas molecule generated through the catalytic action of endogenous nitric oxide synthase isoenzymes upon endogenous Arg[19,51]. NO has been demonstrated the capacity to expedite the healing of diabetic wounds by effectively combatting infection, modulating immune responses, fostering angiogenesis, and stimulating collagen deposition[52,53]. While previous studies

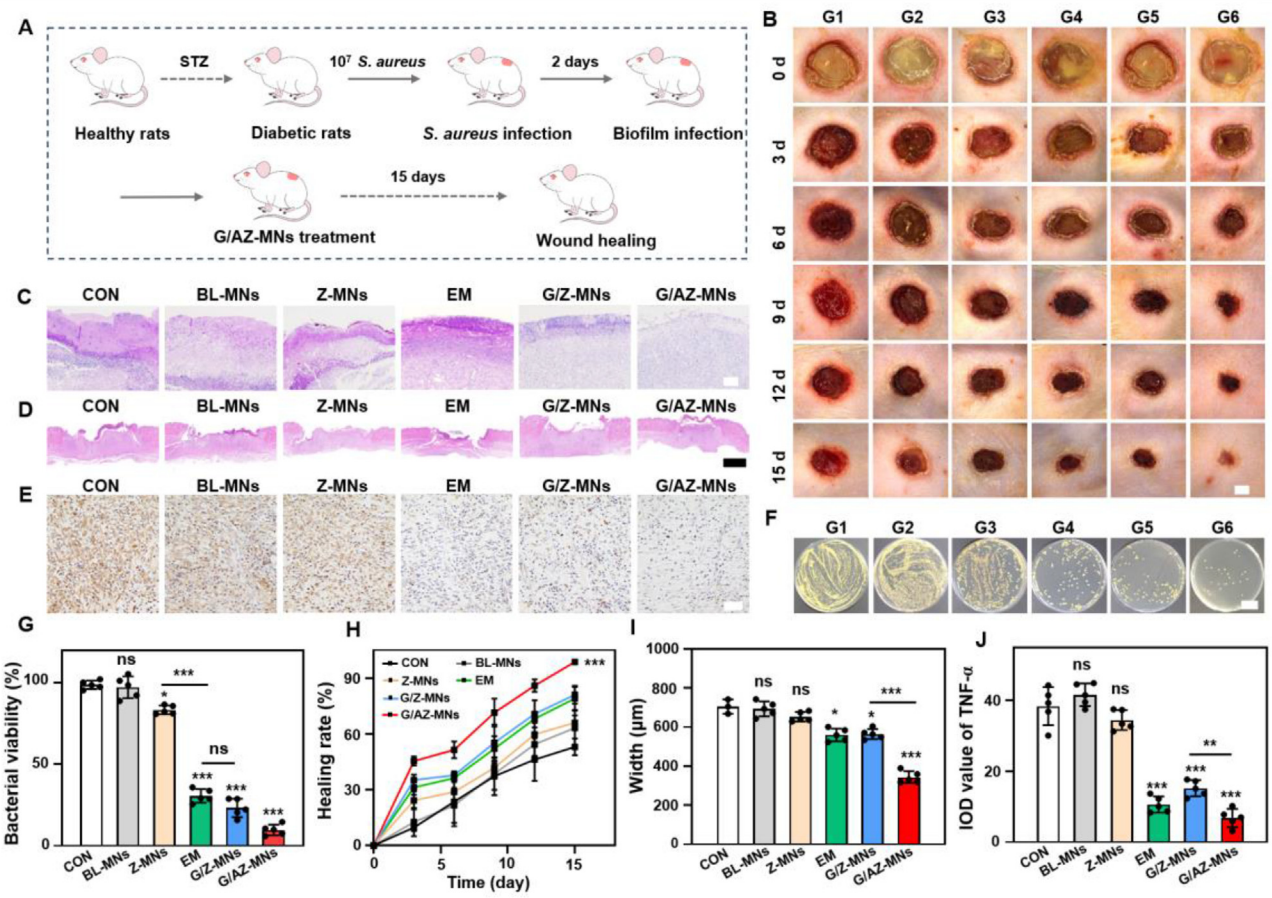

Figure 7 G/AZ-MNs promoting infectious diabetic wound healing. (A) Experimental illustration presenting G/AZ-MNs-mediated wound healing on diabetic rats infected with *S. aureus*. (B) Representative photographs of wounds in SD rats at different time points after different treatments. (G1: CON, G2: BL-MNs, G3: Z-MNs, G4: EM; G5: G/Z-MNs and G6: G/AZ-MNs). Scale bar, 2 mm. (C) Representative Periodic acid-Schiff staining of wound tissues in different groups on Day 6. Scale bar, 100 μm. (D) Representative H&E staining of wound tissues in different groups on Day 6. Scale bar, 2 mm. (E) Representative Immunohistochemistry staining for TNF-α of wound tissues in different groups on Day 6. Scale bar, 50 μm. (F) Photographs of colonies at the wounds on Day 3 in different groups. Scale bar, 20 mm. (G) Quantitative analysis of bacterial viability at the wounds on Day 3 in different groups. (H) Quantitative analysis of the wound healing rate after treatment in different groups. (I) Quantitative analysis of wound width in different groups. (J) Quantitative analysis of TNF-α in different groups measured by integral optical density (IOD). $n = 5$ independent samples, $^{*}P < 0.05$, $^{**}P < 0.01$, $^{***}P < 0.001$, $^{****}P < 0.0001$.

have developed locally releasable NO systems, such as NPs[54], hydrogels[19], and MNs[55], their wide application is greatly hindered by the inability of long-term release[50,56,57]. Furthermore, current therapeutic methods cannot address the issues of localized hyperglycemia, bacterial infection, and persistent inflammation simultaneously.

To overcome the limitations, we introduced a bilayer MN patch (G/AZ-MNs) in this work, which possesses the ability to directly penetrate the formed biofilms with improved drug delivery efficiency, and to adapt to the microenvironment of diabetic wounds for sustained release of the multifunctional NO, thereby facilitating the process of chronic wound healing through its hypoglycemic, antimicrobial, and anti-inflammatory effects. The MN tip layer that encapsulated GOx, was proved to be highly effective in attenuating localized hyperglycemia *via* glucose depletion. Additionally, the NPs present in the MN base layer displayed an acid-responsive degradation behavior, releasing Zn^{2+} to elicit antimicrobial effects. Concurrently, the liberated Arg from the degraded NPs underwent conversion to NO in the presence of H_2O_2, subsequently causing antibacterial effect and inducing macrophage polarization for anti-inflammation. Moreover, we found that the sustained release of NO from G/AZ-MNs could upregulate the expression of VEGF, which promoted neovascularization in wounds. Due to the attractive features, the bilayer MN patch was effective not only in diabetic wounds but also in biofilm-formed diabetic wounds, showing satisfactory therapeutic efficacy in both conditions. To the best of our knowledge, this is the first study to achieve the combination of glucose depletion and sustained release of NO in a single system for accelerating diabetic wound healing.

There are a few limitations of this work. First, the therapeutic efficacy of this bilayer MN patch was only verified in a small

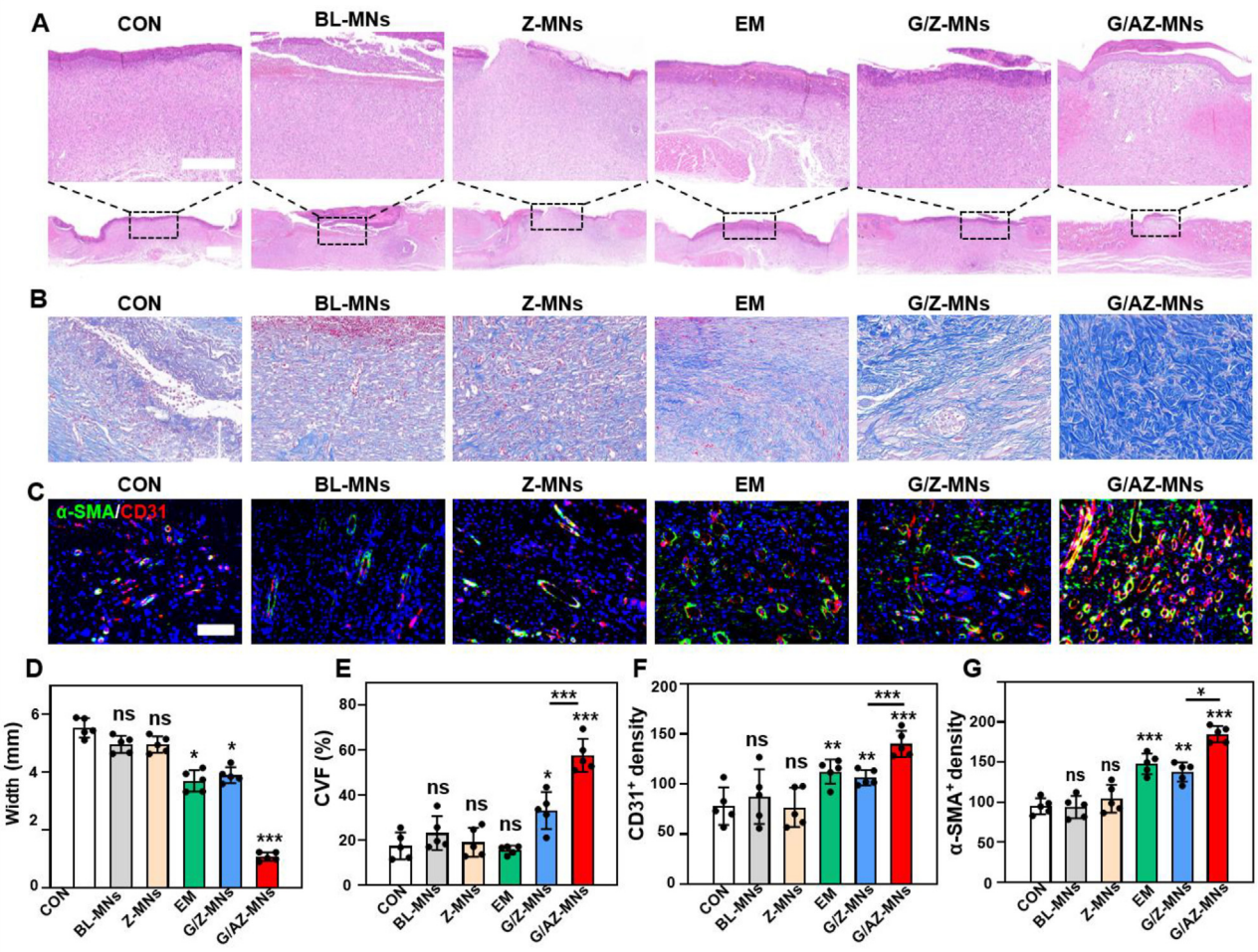

Figure 8 Investigation on tissue regeneration, collagen deposition, and angiogenesis after treatments in different groups. (A) Representative H&E staining of wound tissues in different groups on Day 15. Scale bars, 500 μm (top), 1 mm (bottom). Representative Masson staining (B) and immunofluorescence images of CD31-positive (red) and α-SMA-positive (green) (C) of wound tissues in different groups on Day 15. Scale bars, 100 μm. (D−G) Quantitative analysis of wound width (D), collagen volume fraction (E), and density of CD31+ (F) and α-SMA + on Day 15 (G). $n = 5$ independent samples, $^{*}P < 0.05$, $^{**}P < 0.01$, $^{***}P < 0.001$, $^{****}P < 0.0001$.

number of small animals (*i.e.*, rats), the effect of chronic wound healing promotion also needs to be investigated in a large species, for example, a rabbit or pig model. Second, the fabrication process of the bilayer MN patch is required to be optimized to further improve the storing stability of the GOx enzyme, which can facilitate scaling up the production of the MN patches. Nevertheless, the designed bilayer MN patch that can achieve glucose depletion and sustained NO release for long-acting antibacterial and anti-inflammatory effects simultaneously, provides a promising alternative for patients to better manage chronic wounds. Moreover, the spatiotemporally responsive MN patch can also be readily adopted for transdermal delivery of other therapeutic biomolecules for long-acting treatment of other diseases (*e.g.*, cardiovascular disease) in the future.

Acknowledgments

This work was supported by the National Natural Science Foundation of China (NSFC, Nos. 82373798, 52103182), the Special Project for Significant New Drug Research and Development in the Major National Science and Technology Projects of China (project No. 2020ZX09201007), and Innovation Transformation Research Project of Zhongnan Hospital of Wuhan University (project No. YXCXZH2024003, China).

Author contributions

Yongnian Zeng: Conceptualization, Formal analysis, Investigation, Methodology, Validation, Writing − original draft. Chenyuan Wang: Formal analysis, Investigation, Methodology. Jiapeng Lei: Investigation, Methodology. Xue Jiang: Investigation, Methodology. Kai Lei: Methodology. Yinli Jin: Investigation, Methodology. Tianshu Hao: Methodology. Wen Zhang: Methodology. Jianying Huang: Funding acquisition, Supervision, Writing − review & editing. Wei Li: Conceptualization, Funding acquisition, Project administration, Supervision, Validation, Writing − review & editing.

Conflicts of interest

The authors have no conflicts of interest to declare.

Appendix A. Supporting information

Supporting information to this article can be found online at https://doi.org/10.1016/j.apsb.2024.06.014.

References

1. The L. Diabetes: a defining disease of the 21st century. *Lancet* 2023; **401**:2087.
2. Liu Y, Xia G, Chen Y, Xia H, Xu J, Guo L, et al. Purpurolide C-based microneedle promotes macrophage-mediated diabetic wound healing *via* inhibiting TLR4-MD2 dimerization and MYD88 phosphorylation. *Acta Pharm Sin B* 2023;**13**:5060−73.
3. Armstrong DG, Boulton AJM, Bus SA. Diabetic foot ulcers and their recurrence. *N Engl J Med* 2017;**376**:2367−75.
4. Lazzarini PA, Pacella RE, Armstrong DG, van Netten JJ. Diabetes-related lower-extremity complications are a leading cause of the global burden of disability. *Diabet Med* 2018;**35**:1297−9.
5. McDermott K, Fang M, Boulton AJM, Selvin E, Hicks CW. Etiology, epidemiology, and disparities in the burden of diabetic foot ulcers. *Diabetes Care* 2023;**46**:209−21.
6. Yovera-Aldana M, Sáenz-Bustamante S, Quispe-Landeo Y, Agüero-Zamora R, Salcedo J, Sarria C, et al. Nationwide prevalence and clinical characteristics of inpatient diabetic foot complications: a peruvian multicenter study. *Prim Care Diabetes* 2021;**15**:480−7.
7. Sun BK, Siprashvili Z, Khavari PA. Advances in skin grafting and treatment of cutaneous wounds. *Science* 2014;**346**:941−5.
8. Zhang Y, Wang S, Yang Y, Zhao S, You J, Wang J, et al. Scarless wound healing programmed by core-shell microneedles. *Nat Commun* 2023;**14**:3431.
9. Zhang J, Luo Q, Hu Q, Zhang T, Shi J, Kong L, et al. An injectable bioactive dressing based on platelet-rich plasma and nanoclay: sustained release of deferoxamine to accelerate chronic wound healing. *Acta Pharm Sin B* 2023;**13**:4318−36.
10. Falanga V. Chronic wounds: pathophysiologic and experimental considerations. *J Invest Dermatol* 1993;**100**:721−5.
11. Lobmann R, Ambrosch A, Schultz G, Waldmann K, Schiweck S, Lehnert H. Expression of matrix-metalloproteinases and their inhibitors in the wounds of diabetic and non-diabetic patients. *Diabetologia* 2002;**45**:1011−6.
12. Wang Y, Lv Q, Chen Y, Xu L, Feng M, Xiong Z, et al. Bilayer hydrogel dressing with lysozyme-enhanced photothermal therapy for biofilm eradication and accelerated chronic wound repair. *Acta Pharm Sin B* 2023;**13**:284−97.
13. Liu W, Zhai X, Zhao X, Cai Y, Zhang X, Xu K, et al. Multifunctional double-layer and dual drug-loaded microneedle patch promotes diabetic wound healing. *Adv Healthc Mater* 2023;**12**:2300297.
14. Nguyen TT, Ding D, Wolter WR, Pérez RL, Champion MM, Mahasenan KV, et al. Validation of matrix metalloproteinase-9 (MMP-9) as a novel target for treatment of diabetic foot ulcers in humans and discovery of a potent and selective small-molecule MMP-9 inhibitor that accelerates healing. *J Med Chem* 2018;**61**:8825−37.
15. Zhou W, Duan Z, Zhao J, Fu R, Zhu C, Fan D. Glucose and MMP-9 dual-responsive hydrogel with temperature sensitive self-adaptive shape and controlled drug release accelerates diabetic wound healing. *Bioact Mater* 2022;**17**:1−17.
16. Chen S, Zhu Y, Xu Q, Jiang Q, Chen D, Chen T, et al. Photocatalytic glucose depletion and hydrogen generation for diabetic wound healing. *Nat Commun* 2022;**13**:5684.
17. Ge Y, Rong F, Lu Y, Wang Z, Liu J, Xu F, et al. Glucose oxidase driven hydrogen sulfide-releasing nanocascade for diabetic infection treatment. *Nano Lett* 2023;**23**:6610−8.
18. Singh RK, Yoon DS, Mandakhbayar N, Li C, Kurian AG, Lee NH, et al. Diabetic bone regeneration with nanoceria-tailored scaffolds by recapitulating cellular microenvironment: activating integrin/TGF-β co-signaling of MSCs while relieving oxidative stress. *Biomaterials* 2022;**288**:121732.
19. Malone-Povolny MJ, Maloney SE, Schoenfisch MH. Nitric oxide therapy for diabetic wound healing. *Adv Healthc Mater* 2019;**8**:e1801210.
20. Luo JD, Chen AF. Nitric oxide: a newly discovered function on wound healing. *Acta Pharmacol Sin* 2005;**26**:259−64.
21. Silva SY, Rueda LC, Márquez GA, López M, Smith DJ, Calderón CA, et al. Double blind, randomized, placebo controlled clinical trial for the treatment of diabetic foot ulcers, using a nitric oxide releasing patch: pathon. *Trials* 2007;**8**:26.
22. Edmonds ME, Bodansky HJ, Boulton AJM, Chadwick PJ, Dang CN, D'Costa R, et al. Multicenter, randomized controlled, observer-blinded study of a nitric oxide generating treatment in foot ulcers of patients with diabetes-ProNOx1 study. *Wound Repair Regen* 2018;**26**:228−37.
23. Ahmed R, Augustine R, Chaudhry M, Akhtar UA, Zahid AA, Tariq M, et al. Nitric oxide-releasing biomaterials for promoting wound healing in impaired diabetic wounds: state of the art and recent trends. *Biomed Pharmacother* 2022;**149**:112707.
24. Li Y, Lee PI. Controlled nitric oxide delivery platform based on *S*-nitrosothiol conjugated interpolymer complexes for diabetic wound healing. *Mol Pharm* 2010;**7**:254−66.
25. Hu B, Gao M, Boakye-Yiadom KO, Ho W, Yu W, Xu X, et al. An intrinsically bioactive hydrogel with on-demand drug release behaviors for diabetic wound healing. *Bioact Mater* 2021;**6**:4592−606.
26. Yang L, Zhang D, Li W, Lin H, Ding C, Liu Q, et al. Biofilm microenvironment triggered self-enhancing photodynamic immunomodulatory microneedle for diabetic wound therapy. *Nat Commun* 2023;**14**:7658.
27. Wynn TA. Type 2 cytokines: mechanisms and therapeutic strategies. *Nat Rev Immunol* 2015;**15**:271−82.
28. Chen HH, Fu FS, Chen QW, Zhang Y, Zhang XZ. Two-pronged microbe delivery of nitric oxide and oxygen for diabetic wound healing. *Nano Lett* 2023;**23**:5595−602.
29. Zhou X, Wang H, Zhang J, Li X, Wu Y, Wei Y, et al. Functional poly(ε-caprolactone)/chitosan dressings with nitric oxide-releasing property improve wound healing. *Acta Biomater* 2017;**54**:128−37.
30. Yang J, Chu Z, Jiang Y, Zheng W, Sun J, Xu L, et al. Multifunctional hyaluronic acid microneedle patch embedded by cerium/zinc-based composites for accelerating diabetes wound healing. *Adv Healthc Mater* 2023;**12**:e2300725.
31. Teena R, Dhamodharan U, Ali D, Rajesh K, Ramkumar KM. Genetic polymorphism of the *Nrf2* promoter region (rs35652124) is associated with the risk of diabetic foot ulcers. *Oxid Med Cel Longev* 2020;**2020**:9825028.
32. Xiong Y, Lin Z, Bu P, Yu T, Endo Y, Zhou W, et al. A whole-course-repair system based on neurogenesis-angiogenesis crosstalk and macrophage reprogramming promotes diabetic wound healing. *Adv Mater* 2023;**35**:e2212300.
33. Boniakowski AE, Kimball AS, Jacobs BN, Kunkel SL, Gallagher KA. Macrophage-mediated inflammation in normal and diabetic wound healing. *J Immunol* 2017;**199**:17−24.
34. Dong RN, Guo BL. Smart wound dressings for wound healing. *Nano Today* 2021;**41**:101290.
35. McLister A, McHugh J, Cundell J, Davis J. New developments in smart bandage technologies for wound diagnostics. *Adv Mater* 2016;**28**:5732−7.
36. Falanga V. Wound healing and its impairment in the diabetic foot. *Lancet* 2005;**366**:1736−43.
37. Werner S, Breeden M, Hubner G, Greenhalgh DG, Longaker MT. Induction of keratinocyte growth-factor expression is reduced and delayed during wound-healing in the genetically diabetic mouse. *J Invest Dermatol* 1994;**103**:469−73.
38. Zhu YX, Cankova Z, Iwanaszko M, Lichtor S, Mrksich M, Ameer GA. Potent laminin-inspired antioxidant regenerative dressing accelerates

wound healing in diabetes. *Proc Natl Acad Sci U S A* 2018;**115**:6816−21.
39. Ohki M, Ohki Y, Ishihara M, Nishida C, Tashiro Y, Akiyama H, et al. Tissue type plasminogen activator regulates myeloid-cell dependent neoangiogenesis during tissue regeneration. *Blood* 2010;**115**:4302−12.
40. Darvishi S, Tavakoli S, Kharaziha M, Girault HH, Kaminski CF, Mela I. Advances in the sensing and treatment of wound biofilms. *Angew Chem Int Ed Engl* 2022;**61**:e202112218.
41. Zhang X, Wang Z, Jiang H, Zeng H, An N, Liu B, et al. Self-powered enzyme-linked microneedle patch for scar-prevention healing of diabetic wounds. *Sci Adv* 2023;**9**:eadh1415.
42. Li S, Wang X, Yan Z, Wang T, Chen Z, Song H, et al. Microneedle patches with antimicrobial and immunomodulating properties for infected wound healing. *Adv Sci* 2023;**10**:e2300576.
43. Wang P, Wu J, Yang H, Liu H, Yao T, Liu C, et al. Intelligent microneedle patch with prolonged local release of hydrogen and magnesium ions for diabetic wound healing. *Bioact Mater* 2023;**24**:463−76.
44. Guan Y, Niu H, Liu Z, Dang Y, Shen J, Zayed M, et al. Sustained oxygenation accelerates diabetic wound healing by promoting epithelialization and angiogenesis and decreasing inflammation. *Sci Adv* 2021;**7**:eabj0153.
45. Li Y, Fu R, Duan Z, Zhu C, Fan D. Artificial nonenzymatic antioxidant mxene nanosheet-anchored injectable hydrogel as a mild photothermal-controlled oxygen release platform for diabetic wound healing. *ACS Nano* 2022;**16**:7486−502.
46. Zhang X, Chen G, Liu Y, Sun L, Sun L, Zhao Y. Black phosphorus-loaded separable microneedles as responsive oxygen delivery carriers for wound healing. *ACS Nano* 2020;**14**:5901−8.
47. Wu H, Yang P, Li A, Jin X, Zhang Z, Lv H. *Chlorella* sp.-ameliorated undesirable microenvironment promotes diabetic wound healing. *Acta Pharm Sin B* 2023;**13**:410−24.
48. Tu C, Lu H, Zhou T, Zhang W, Deng L, Cao W, et al. Promoting the healing of infected diabetic wound by an anti-bacterial and nano-enzyme-containing hydrogel with inflammation-suppressing, ROS-scavenging, oxygen and nitric oxide-generating properties. *Biomaterials* 2022;**286**:121597.
49. Yang Y, Li M, Pan G, Chen J, Guo B. Multiple stimuli-responsive nanozyme-based cryogels with controlled NO release as self-adaptive wound dressing for infected wound healing. *Adv Funct Mater* 2023;**33**:2214089.
50. Yao S, Wang Y, Chi J, Yu Y, Zhao Y, Luo Y, et al. Porous MOF microneedle array patch with photothermal responsive nitric oxide delivery for wound healing. *Adv Sci* 2022;**9**:e2103449.
51. Finkelman BS, Putt M, Wang T, Wang L, Narayan H, Domchek S, et al. Arginine-nitric oxide metabolites and cardiac dysfunction in patients with breast cancer. *J Am Coll Cardiol* 2017;**70**:152−62.
52. Farah C, Michel LYM, Balligand JL. Nitric oxide signalling in cardiovascular health and disease. *Nat Rev Cardiol* 2018;**15**:292−316.
53. Lundberg JO, Weitzberg E, Gladwin MT. The nitrate-nitrite-nitric oxide pathway in physiology and therapeutics. *Nat Rev Drug Discov* 2008;**7**:156−67.
54. Bai Q, Han K, Dong K, Zheng C, Zhang Y, Long Q, et al. Potential applications of nanomaterials and technology for diabetic wound healing. *Int J Nanomedicine* 2020;**15**:9717−43.
55. Liu A, Wang Q, Zhao Z, Wu R, Wang M, Li J, et al. Nitric oxide nanomotor driving exosomes-loaded microneedles for achilles tendinopathy healing. *ACS Nano* 2021;**15**:13339−50.
56. Zhang P, Li Y, Tang Y, Shen H, Li J, Yi Z, et al. Copper-based metal-organic framework as a controllable nitric oxide-releasing vehicle for enhanced diabetic wound healing. *ACS Appl Mater Inter* 2020;**12**:18319−31.
57. Zhou X, Zhao B, Wang L, Yang L, Chen H, Chen W, et al. A glucose-responsive nitric oxide release hydrogel for infected diabetic wounds treatment. *J Control Release* 2023;**359**:147−60.